ARTICLE

Check for updates

Study of the Ballistic Impact Behavior of Protective Multi-Layer Composite Armor

Dongsheng Jia, Yingjie Xu[*], Liangdi Wang, Jihong Zhu and Weihong Zhang

State IJR Center of Aerospace Design and Additive Manufacturing, Northwestern Polytechnical University, Xi'an, 710072, China

*Corresponding Author: Yingjie Xu. Email: xu.yingjie@nwpu.edu.cn

ABSTRACT

The abalone shell, a composite material whose cross-section is composed of inorganic and organic layers, has high strength and toughness. Inspired by the abalone shell, several multi-layer composite plates with different layer sequences and thicknesses are studied as bullet-proof material in this paper. To investigate the ballistic performance of this multi-layer structure, the complete characterization model and related material parameters of large deformation, failure and fracture of Al_2O_3 ceramics and Carbon Fiber Reinforced Polymer (CFRP) are studied. Then, 3D finite element models of the proposed composite plates with different layer sequences and thicknesses impacted by a 12.7 mm armor-piercing incendiary (API) are built using Abaqus to predict failure. The simulation results show that the CFRP/Al_2O_3 ceramic/Ultrahigh Molecular Weight Polyethylene (UHMWPE)/CFRP (1 mm/4 mm/4 mm/1 mm) composite is the optimized stack of layers. The simulation results under specified layer sequence and thickness have a reasonable correlation with the experimental results and reflect the failure and fracture of the multi-layer composite protective armor.

Nomenclature

σ^*	Normalized equivalent stress
D	Damage
σ_i^*	Equivalent intact stress
σ_f^*	Equivalent fracture stress
σ_{HEL}	Stress at hugoniot elastic limit (HEL)
σ	Actual equivalent stress
σ_i^{max}	The ultimate stress of intact
σ_f^{max}	The ultimate stress of fracture
P_{HEL}	Pressure at hugoniot elastic limit (HEL)
P^*	Normalized pressure
P	Hydrostatic pressure
T^*	Normalized maximum uniaxial hydrostatic pressure

T	Maximum uniaxial hydrostatic pressure
$\dot{\varepsilon}^*$	Strain rate
$\dot{\varepsilon}_0$	Reference strain rate
$\dot{\varepsilon}^{\overline{ac}}$	Actual strain rate
$\Delta\varepsilon^{\overline{pl}}$	Increment of equivalent plastic strain
$\varepsilon_f^{\overline{pl}}$	Equivalent plastic strain
$A_{1\sim2}$	Material property constant
$\varepsilon_{fmin}^{\overline{pl}}$	The lower limit of fracture plastic strain
$\varepsilon_{fmax}^{\overline{pl}}$	The upper limit of fracture plastic strain
ρ	Current density
ρ_0	Initial density
$D_{1\sim3}$	Material property constant
ΔP	Pressure increment
ΔU	Elastic energy increment
k	Loss percentage of elastic energy
t	Current time
$t + \Delta t$	Updated time
E_{11}	Longitudinal tensile modulus
E_{22}	Transverse elastic modulus (Interlayer)
D_{12}	Shear modulus in plane 1–2 (In-plane)
D_{23}	Shear modulus in plane 2–3 (Interlayer)
μ_{12}	Poisson's ratio
G_{m}	Resin fracture energy
G_{f}	Fiber fracture energy
d_{ft}	Tensile fiber damage factor
d_{fc}	Compressive fiber damage factor
d_{mt}	Tensile composite matrix damage factor
d_{mc}	Compressive composite matrix damage factor
F	Strength
S	Shear
C	Compression
G	Tensile
x	Orthogonal direction x
y	Orthogonal direction y
α	Material property coefficient 1 adjusting the influence of shear stress
β	Material property coefficient 2 adjusting the influence of shear stress

1 Introduction

The demand for lightweight, high-performance materials for applications in the defence industry, aeronautical and civil engineering is growing quickly with the development of science and human society [1–5]. Thus, structural material design to satisfy the requirement of lightweight on the one hand and high ballistic-proof performance on the other hand becomes a challenge. In this situation, bionic materials, such as desert lizards, bone, shells, and bamboo with lightweight and high-strength properties, have inspired much research in structural materials design by imitating the structures and features of natural organisms since the natural materials after millions of years of evolutionary

developments usually have higher performance and better structures with relatively weak materials [6–8].

Among those bionic materials, abalone-like structures have obtained remarkable attention for the design of impact-resistant material [9–11]. The white clam shell is studied concerning the microstructure and mechanical properties. It was demonstrated that the microstructure characteristics and the diversity of material properties among the different layers enhanced the white calm shell's mechanical and crack arrest properties [9,12,13]. The white clam shell comprises 95% lamellar calcium carbonate ($CaCO_3$) and 5% organic matter (protein and polysaccharide). The mineralized biological materials have relatively higher compressive strength, while the organic materials have higher ductility, toughness, and tensile strength because they are fibrous. Thus, the mineralized materials serve better in compression and organic materials in tension working conditions. In other words, mineralized components provide load-bearing capacity, whereas organic materials provide toughness and viscoelastic damping [10]. Although the organic material in the white clamshell is only 5%, it controls the configuration of crystals, thus playing an essential role in improving the toughness [14,15]. The toughness of the white calm shell can reach more than 3000 times that of a single mineralized layer. Thus, many studies have demonstrated the better toughness and strength of multi-layered structures with alternating soft and hard phases [16,17]. Wang et al. [18] fabricated a layered cross-structure ceramic tile bonded with resin and impacted it with a drop hammer. The experimental results show that the layered ceramic tiles can limit crack propagation and deflect cracks. Regarding numerical simulation, Grujicic et al. [19] established a B_4C/polyurea composite model to study the performance under the impact of solid cylinder projectiles. The results show that the B_4C/polyurea composite has a better ballistic protection effect than the single B_4C material. The metals are also chosen as a layer of the lamellar shell in the bionic structure design [20,21]. Flores-Johnson et al. bonded the 7075 aluminium alloy blocks with epoxy resin to create certain surface fluctuation and interface bonding strength. The numerical simulation showed that the energy absorption capacity of the laminated aluminium alloy plate is much better than that of the whole plate with the same thickness. The metal hybrid method can effectively solve the problem of low energy absorption efficiency of Carbon Fiber Reinforced Polymer (CFRP) under lateral crushing load, and the application prospect of the hybrid tube can be better explored through the related crashworthiness design. More importantly, the lateral crushing behavior of carbon fiber reinforced plastic/aluminium (CFRP/AL) hybrid tubes under different parameter configurations were analysed to improve the mechanical performance of CFRP tubes significantly [22–25]. Vecchio [26] prepared a high-performance Ti/Al_3Ti composite material using the layer self-assembly method. The crack growth curve of Ti/Al3Ti composite material is similar to that of titanium alloy but with higher stiffness and lower density. Chandler et al. [27] prepared the biomimetic polyvinyl alcohol (PVA)/montmorillonite (MMT) nanomembrane materials and used them as the surface layer of high-performance cement materials. The composite materials showed excellent impact resistance. Despite the various research in the literature focusing on the mechanical properties of the bionic structure, the impact-resistant armor inspired by inorganic-organic multi-layer bionic configuration is very limited.

Apart from the above inorganic-organic multi-layer bionic configuration, the choice of the layers' material is another aspect of improving the performance of the protective armor [28]. The traditional protective armor was based on pure metals, such as steel and aluminium [29,30]. Later, ceramic/fiber composites are proposed. The ceramic material has high compressive strength to crush the bullet, and the fiber composite material as the back plate can absorb the remaining energy of the projectile. Fiber composite materials used to manufacture armor structures are mainly high-modulus, high-temperature resistant, high-performance fibers with high fracture strain [31]. The

protective performance of this ceramic/fiber composite armour is significantly improved compared to the traditional material. Also, lightweight bullet-proof armor materials, such as Al_2O_3, aluminium alloy, woven and Ultrahigh Molecular Weight Polyethylene (UHMWPE) fiber, have a convenient process, noticeable weight reduction, and good impact resistance compared with traditional metal bullet-proof materials [31,32]. UHMWPE fiber is a high-performance fiber with low density, high modulus and high specific strength. Thus, it has a remarkable ability to absorb impact energy, making it widely used in bullet-proof products [33,34]. Previous research is mainly focused on armour composed of pure metals or few materials. However, owing to its complexity, multi-layer amour with different layer sequences and thicknesses should be studied computationally and experimentally to build the theory of designing multi-layer amour.

Recent literature studied the design of armour under bullet impact from other perspectives [35]. A theoretical impacting model of the ceramics/aluminium composite armour is built to analysis the bullet-proof performance of armour rather than describe the armour as a single component [36]. The non-equivalent mechanical properties are performed and the fracture and erosion of ceramic under high strain rate and pressure of ceramic in the armour during perforation have been considered [37]. The ballistic performance of moderately thick (relatively thick compared to projectiles' diameter) metallic armour is studied and the existing incompatible ballistic results are analysed [38]. A cartography showing injection regions of the projectile is investigated to analysis of the material damage [39]. A surface-based cohesive material model using traction-separation constitutive law between adjacent layers is built to study the amours' ballistic penetration behaviors [40]. An alumina/ceramic armor with strong confinement on the penetration process of the projectile is performed for testing the influence of constraint [41]. The impact tests performed with incendiary bullets of 7.62 mm caliber against multi-layer armor containing alloy and ultra-high-molecular-weight polyethylene are presented [42]. The ballistic performance of the armor against a flat-nosed projectile was investigated experimentally and numerically [43]. The role of the hot curing pressure on the influence of the bullet-proof performance of composite armor is quantified and included in finite element models [44]. The dynamic response of a sandwich armor, constructed with Kevlar/carbon fiber/epoxy as top and bottom skins and the core of the triangular corrugated aluminium structure is studied [45]. In our previous study [46], an origami shield composed of modular composite plates has been designed and manufactured. However, although the above-mentioned studies have analyzed the armour from different perspectives, such as the constraint method, bullet shape, curing processes, and failure models, few studies have focused on the bio-inspired inorganic-organic multi-layer mechanism and a consensus regarding the design of modular composite plates with different layer sequences and thicknesses is lacking. In other words, research in the literature did not systematically optimize layer stacks (layer thickness and sequence) with different strength, toughness, stiffness and density properties. This work aims to assess the bullet-proof performance of abalone-like Al_2O_3 ceramics/UHMWPE/CFRP composite armour by finite element model and ballistic test. The complete characterization model and related parameters of large material deformation, failure and fracture of Al_2O_3 ceramics and CFRP multi-layer composite is introduced. Based on the different properties of Al_2O_3 ceramics, UHMWPE and CFRP in hardness, strength and energy absorption, 3D finite element models of a multi-layer protective composite plate with different layer thicknesses and sequences are established. Then, a finite-element analysis (transient, nonlinear dynamic) is performed to simulate the ballistic impact and optimize its layer stacks scheme inspired by an abalone shell. The physical samples of the composite plate are impacted by a gun to verify its bullet-proof performance for use as armour.

This work provides design theory for developing lightweight, high-performance, multi-layer composite protective armours. Based on the analysis of the above research, the protective armour

is designed in a multi-layer composite plate. The material models and the finite element models to simulate the bullet-proof performance are presented in Section 2. The fabrication process and ballistic experiment are presented and discussed in Section 3. The main conclusion is summarized in Section 4.

2 Material Models and Finite Element Modelling

2.1 Material Models

The constitutive models of Al_2O_3 ceramics and carbon fibre composites were established and compiled into the user's material subroutine in Abaqus to accurately simulate material properties during the impact. Considering the mechanical properties at high strain rates and the evolution characteristics of damage and fracture, the characterization model of the composites is divided into two parts: First, the material properties model at the high strain before failure is established. Then, a description function including elastic energy, plastic strain energy and damage parameters after the damage is constructed and combined with the basic characterization model. Finally, a complete characterization model considering large deformations and failure under high-speed impact is obtained based on the aforementioned two parts.

2.1.1 JH-2 Constitutive Model of Al_2O_3 Ceramics

The Johnson-Holmquist constitutive model (JH-2 model) [47] consists of three main parts: (1) the materials' strength is expressed in a smooth function of pressure-related yield surface; (2) the transition from the undamaged state to the start of damaged state to the final fracture state [48]; (3) equation of state (EOS) of pressure-density relationship considering expansion effect. The constitutive model is illustrated as follows.

The Relation between Stress and Strength

The normalized equivalent stress σ^* is represented by the equivalent of Von Mises stress:

$$\sigma^* = \sigma_i^* - D\left(\sigma_i^* - \sigma_f^*\right), \tag{1}$$

where σ_i^* is the equivalent intact stress, D is the damage factor and σ_f^* is the equivalent fracture stress.

The aforementioned equivalent stress, including σ_i^*, σ_f^* and σ^*, can be generally written as $\sigma^* = \sigma/\sigma_{HEL}$, where σ_{HEL} is the stress when the dynamic uniaxial strain load reaches the limit of elastic response, named Hugoniot Elastic Limit (HEL), σ is the actual equivalent stress.

It is assumed that equivalent intact σ_i^* and fracture stresses σ_f^* can be calculated by the function of strain and pressure rates:

$$\sigma_i^* = I\left(P^* + T^*\right)^N \left(1 + K \ln \dot{\varepsilon}^*\right) \leq \sigma_i^{\max},$$
$$\sigma_f^* = J\left(P^*\right)^M \left(1 + K \ln \dot{\varepsilon}^*\right) \leq \sigma_f^{\max}, \tag{2}$$

where M, N, I, J and K are material property constants, σ_i^{max} and σ_f^{max} is the ultimate stress of intact and fracture, respectively. The normalized pressure is described by $P^* = P/P_{HEL}$, where P_{HEL} is the pressure of the material at the HEL and P is the hydrostatic pressure. The normalized maximum uniaxial hydrostatic pressure is defined by $T^* = T/P_{HEL}$, where T is the maximum uniaxial hydrostatic pressure. The strain rate is calculated by $\dot{\varepsilon}^* = \dot{\varepsilon}^{\overline{ac}}/\dot{\varepsilon}_0$, where $\dot{\varepsilon}_0$ is the reference strain rate, $\dot{\varepsilon}^{\overline{ac}}$ is the actual strain rate.

Damage Model

The damage accumulation criterion is similar to the Johnson-Cook fracture model [49] and the JH-1 model [50]. The damage D is related to plastic strain and can be calculated by:

$$D = \sum \frac{\Delta \varepsilon^{\overline{pl}}}{\varepsilon_f^{\overline{pl}}(P)}, \tag{3}$$

where $\Delta \varepsilon^{\overline{pl}}$ is the increment of equivalent plastic strain. The pressure is assumed to be constant. The equivalent plastic strain before fracture $\varepsilon_f^{\overline{pl}}(P)$ is calculated by:

$$\varepsilon_f^{\overline{pl}} = A_1 (P^* + T^*)^{A_2}, \varepsilon_{f,\min}^{\overline{pl}} \leq \varepsilon_f^{\overline{pl}} \leq \varepsilon_{f,\max}^{\overline{pl}}, \tag{4}$$

where A_1 and A_2 are the material property constants. $\varepsilon_{fmin}^{\overline{pl}}$ and $\varepsilon_{fmax}^{\overline{pl}}$ are the lower and upper limits of fracture plastic strain, respectively. P^* is the normalized pressure, T^* is the normalized maximum uniaxial hydrostatic pressure. It is assumed that the increase of material damage variable is continuous.

Compressive Stress

The hydrostatic pressure P during the elastic state is calculated by:

$$P = \begin{cases} D_1\mu + D_2\mu^2 + D_3\mu^3 & \mu \geq 0 \quad (\text{compression}) \\ D_1\mu & \mu < 0 \quad (\text{expansion}) \end{cases}, \tag{5}$$

where $\mu = \rho/\rho_0 - 1$, ρ is the current density, ρ_0 is the initial density, D_1, D_2 and D_3 are the material property constants.

Taking into account the bulking after the damage, the pressure hydrostatic P is reformulated by:

$$P = D_1\mu + D_2\mu^2 + D_3\mu^3 + \Delta P, \mu \geq 0 \ (\text{compression}). \tag{6}$$

where the pressure increment ΔP is described by the function of energy. Changing from the intact state to the complete fracture state, the elastic energy decreases ΔU and is gradually converted into internal energy by increasing pressure ΔP, when the material is damaged. The updated ΔP can be calculated by:

$$\Delta P_{t+\Delta t} = -D_1\mu_{t+\Delta t} + \sqrt{(D_1\mu_{t+\Delta t} + \Delta P_t)^2 + 2kD_1\Delta U}, \tag{7}$$

where k represents the loss percentage of elastic energy, $\Delta P_{t+\Delta t}$ and $\mu_{t+\Delta t}$ are the updated ΔP and μ, respectively, t is the current time and $t + \Delta t$ is the updated time.

2.1.2 The Constitutive Model of Carbon Fiber Reinforced Polymer (CFRP) Composites

Elastic Model

The matrix of CFRP is assumed to have a bilinear elastic-plastic stress-strain behavior. Before the stress reaches the initial yield limit, the matrix behaves homogenously and linearly. After the stress reaches the initial yield limit, the matrix behaves linearly plastically and is assumed to be isotropic [51].

　　　Yarns of CFRP are assumed to be isotropic transversely. Its elastic properties can be calculated from initial elastic engineering constants (E_{11}, E_{22}, G_{12}, G_{13}, μ_{12} and μ_{23}) [52,53]:

$$E_{11} = V_f E_{f_{11}} + \left(1 - V_f\right) E_m$$

$$E_{22} = E_{33} = \frac{E_m}{1 - \sqrt{V_f}\left(1 - \frac{E_m}{E_{f_{22}}}\right)}$$

$$G_{12} = G_{13} = \frac{G_m}{1 - \sqrt{V_f}\left(1 - \frac{G_m}{G_{f_{12}}}\right)}$$

$$G_{23} = \frac{G_m}{1 - \sqrt{V_f}\left(1 - \frac{G_m}{G_{f_{23}}}\right)} \tag{8}$$

$$\mu_{12} = \mu_{13} = V_f \mu_{f_{12}} + \left(1 - V_f\right) \mu_m$$

$$\mu_{23} = \frac{E_{22}}{2 G_{23}} - 1,$$

where $E_{f_{11}}$ and $E_{f_{22}}$ are the fibre's elastic moduli in the directions of longitudinal and transverse, respectively, $G_{f_{12}}$ and $G_{f_{23}}$ are the shear moduli in plane 1–2 and 2–3, respectively, μ_{12} and μ_{23} are the Poisson's ratio in plane 1–2 and 2–3, respectively, E_m, G_m and μ_m are the elastic modulus, shear modulus and Poisson's ratio of the matrix. V_f is the fiber volume fraction of yarn.

　　　Based on the above initial elastic engineering constants, the constitutive model of transversely isotropic material in the elastic phase is given below:

$$\boldsymbol{\varepsilon} = \mathbf{S}_{\text{full}} \boldsymbol{\sigma}, \tag{9}$$

where $\mathbf{S}_{\text{full}}$ is the elastic matrix before damage, $\boldsymbol{\sigma}$ and $\boldsymbol{\varepsilon}$ are the stress and strain vectors. The elastic matrix can be calculated by [47]:

$$\mathbf{S}_{\text{full}} = \begin{bmatrix} \dfrac{1}{E_{11}} & -\dfrac{\mu_{21}}{E_{22}} & -\dfrac{\mu_{31}}{E_{33}} & 0 & 0 & 0 \\ -\dfrac{\mu_{12}}{E_{11}} & \dfrac{1}{E_{22}} & -\dfrac{\mu_{32}}{E_{33}} & 0 & 0 & 0 \\ -\dfrac{\mu_{13}}{E_{11}} & -\dfrac{\mu_{23}}{E_{22}} & \dfrac{1}{E_{33}} & 0 & 0 & 0 \\ 0 & 0 & 0 & \dfrac{1}{G_{12}} & 0 & 0 \\ 0 & 0 & 0 & 0 & \dfrac{1}{G_{13}} & 0 \\ 0 & 0 & 0 & 0 & 0 & \dfrac{1}{G_{23}} \end{bmatrix}, \tag{10}$$

　　　Thus, $\mathbf{S}_{\text{full}}$ can be calculated from the initial elastic engineering constants.

Damage Model

　　　The final failure of the material is caused by the accumulation of damage. Damage mechanisms of the 3D Hashin [54,55] are introduced in this paper to predict the failure behavior. According to the damage directions of the fiber's longitudinal and matrix's transverse, damage mechanisms of the 3D Hashin are indicated by tensile fiber damage factors d_{ft}, compressive fiber damage factors d_{fc}, the tensile composite matrix damage factors d_{mt} and compressive composite matrix damage factors d_{mc}.

Tensile fibre damage initiation criterion:

$$d_{ft} = \left(\frac{\sigma_{xx}}{F_{xG}}\right)^2 + \alpha \left(\frac{\sigma_{xy}}{F_{xS}}\right)^2 + \beta \left(\frac{\sigma_{xz}}{F_{yS}}\right)^2, \text{ if } \sigma_{xx} > 0,$$ (11)

Compressive fibre damage initiation criterion:

$$d_{fc} = \left(\frac{\sigma_{xx}}{F_{xC}}\right)^2, \text{ if } \sigma_{xx} < 0,$$ (12)

Tensile composite matrix damage initiation criterion:

$$d_{mt} = \left(\frac{\sigma_{yy} + \sigma_{zz}}{F_{yG}}\right)^2 + \frac{\sigma_{yy}^2 - \sigma_{yy}\sigma_{zz}}{F_{yS}^2} + \left(\frac{\sigma_{xy}}{F_{xS}}\right)^2 + \left(\frac{\sigma_{yz}}{F_{yS}}\right)^2,$$ (13)

Compressive composite matrix damage initiation criterion:

$$d_{mc} = \frac{1}{F_{yC}} \left[\left(\frac{F_{yC}}{2F_{yS}}\right)^2 - 1 \right] (\sigma_{yy} + \sigma_{zz}) + \left(\frac{\sigma_{yy} + \sigma_{zz}}{2F_{yS}}\right)^2 + \frac{\sigma_{yz}^2 - \sigma_{yy}\sigma_{zz}}{F_{yS}} + \left(\frac{\sigma_{xy}}{F_{xS}}\right)^2 + \left(\frac{\sigma_{xz}}{F_{zS}}\right)^2,$$ (14)

where F and σ are strength and stress, subscripts S, C and G represent shear, compression and tensile of yarns, subscripts x, y and z represent three orthogonal directions, α and β are material property coefficients adjusting the influence of shear stress and is set to 1, F_{xC}, F_{yG} and F_{yC} are the yarn compressive failure strength, yarn transverse tensile failure strength and yarn transverse compressive failure, respectively. Only when all the factors in damage mechanisms (d_{ft}, d_{fc}, d_m) are smaller than 1, the material is judged not damaged.

2.2 Finite Element Model

In order to study the bullet-proof performance of composite plates with different sequences and thicknesses, the composite plates were impacted by a 12.7 mm armour-piercing projectile (API) with a velocity of 400 m/s [38]. The geometry model was generated and pre-processed by the commercial software SolidWorks 2018. Based on the constitutive relation model and data provided in Section 2.1, the finite element model of the target plate is established by Abaqus/Explicit (Version 6.11). In the finite element model, the 100 mm × 100 mm × 10 mm multi-layer composite square plates (see Fig. 1a) with different sequences and thicknesses (see Fig. 2) are set as test samples. The location of displacement recording point P is shown in Fig. 1a. Point P, rather than the central point at the back side of the UHMWPE plate (the point of impact), is selected for displacement comparison in Case 1~4 because the material at the impact point will splash and not reflect the deformation of the plate. Inspired by the inorganic-organic multi-layer bionic configuration, the thickness and sequences of each material are set in Table 1. The multi-layer composite plates are composed of three materials: CFRP, Al$_2$O$_3$ ceramic and UHMWPE. The grids are composed of reduced-integration linear hexahedral elements (C3D8R). It is assumed that the layers with different materials are tied together using Tie Constraints in Abaqus. The multi-layer composite plate is clamped at the edge boundaries. The geometry model of the bullet is shown in Fig. 1b. The physical properties of the materials used in the multi-layer composite samples and the bullet are listed in Tables 2–4. Case 1~4 is tested to analyse the influence of layer sequence and thickness on the impact resistance under the same impact. The impact was simulated in six hours using a 3.19 GHz 16-Core 12th Gen Intel Core i9, running Windows 10 Professional 19044.2364.
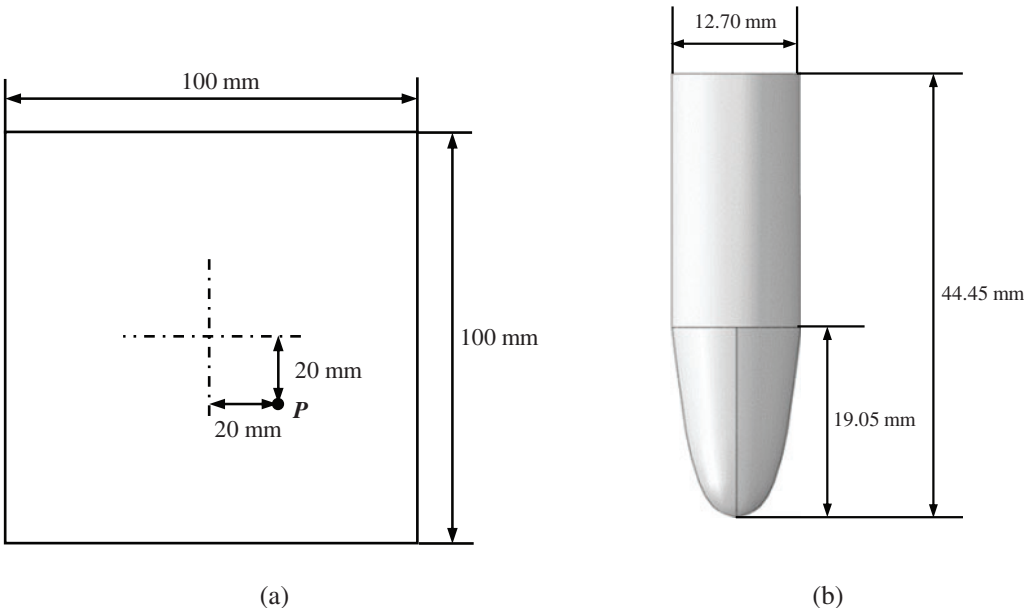
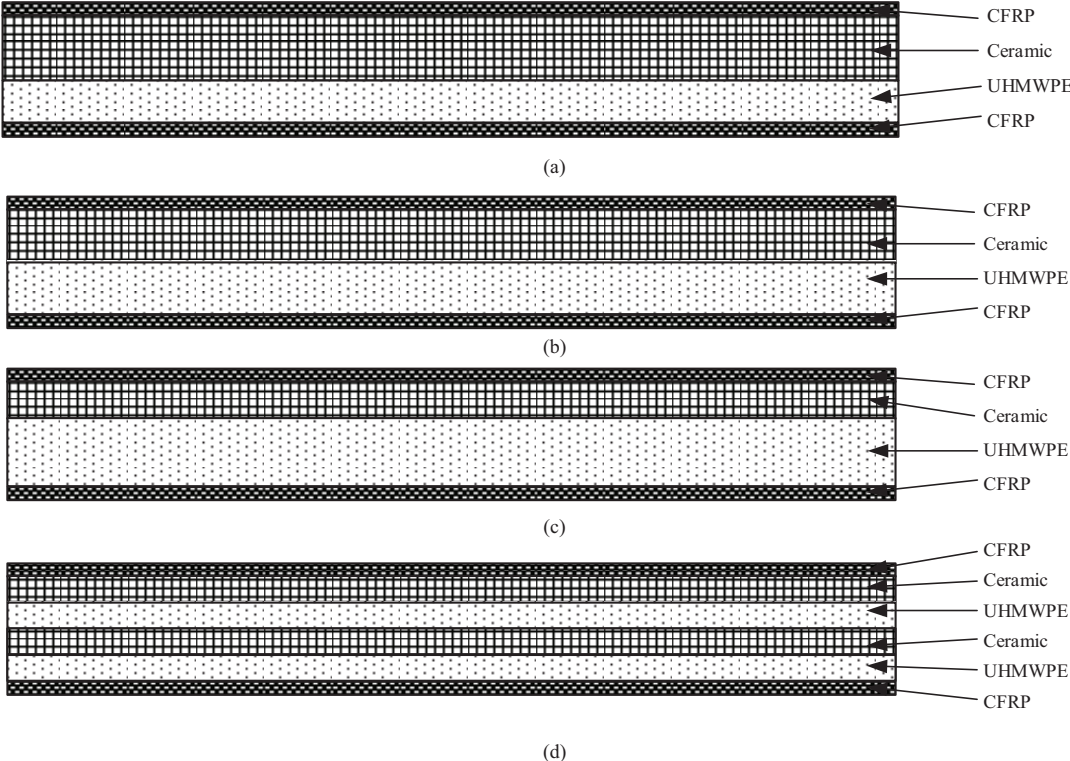**Figure 1:** The geometry model and dimensions: (a) The composite plate, (b) The bullet

Figure 2: Composite stack diagram of Case 1~4: (a) Case 1, (b) Case 2, (c) Case 3, (d) Case 4

Table 1: Stacking sequence and thickness of each layer in Case 1~4

Case 1		Case 2		Case 3		Case 4	
CFRP	1 mm	CFRP	1 mm	CFRP	1 mm	CFRP	1 mm
Ceramics	5 mm	Ceramics	4 mm	Ceramics	3 mm	Ceramics	2 mm
UHMWPE	3 mm	UHMWPE	4 mm	UHMWPE	5 mm	UHMWPE	2 mm
CFRP	1 mm	CFRP	1 mm	CFRP	1 mm	Ceramics	2 mm
						UHMWPE	2 mm
						CFRP	1 mm

Table 2: Material properties of Al_2O_3 Ceramic

Item	Value
Density (kg/m³)	3700
Shear modulus (GPa)	90.16
I	0.93
J	0.31
K	0.00
M	0.60
N	0.60
Reference strain rate $\dot{\varepsilon}_0$	1.00
σ_{HEL} (GPa)	2.79
P_{HEL} (GPa)	1.46
A_1	0.005
A_2	1.00
D_1 (GPa)	130.95
D_2 (GPa)	0.00
D_3 (GPa)	0.00
Loss percentage of elastic energy k	1.00

Table 3: Material properties of carbon fibers and resin matrix

	Carbon fibres	Resin matrix
Longitudinal tensile modulus (0°) E_{11} (GPa)	230	3.5
Longitudinal compressive modulus (90°) E_{11} (GPa)	180	3.5
Transverse elastic modulus (Interlayer) E_{22} (GPa)	40	3.5
Shear modulus in plane 1–2 (In-plane) D_{12} (GPa)	24	1.3
Shear modulus in plane 2–3 (Interlayer) D_{23} (GPa)	14.3	1.3
Poisson's ratio μ_{12}	0.26	0.35

(Continued)

Table 3 (continued)

	Carbon fibres	Resin matrix
Tensile Strength F_G (MPa)	4900	80
Compressive Strength F_C (MPa)	2470	241
Shear strength F_s (MPa)	/	60
Resin fracture energy G_m (N/mm)	8.0	/
Fiber fracture energy G_f (N/mm)	/	1.5

Table 4: Material properties of UHMWPE and steel

	UHMWPE	Steel
Density (kg/m³)	2700	7850
Young's modulus (GPa)	2.45	210
Poisson' ratio	0.46	0.3

The structures in Case 1~4 are meshed with C3D8R elements, as shown in Fig. 3. The number of elements in Case 1~4 is 194087, 196304, 194087 and 196304, respectively. The four sides of the composite samples are fixed. The bullet is applied to the predefined central field of plates. The velocity of the bullet is 400 m/s perpendicular to the plate surface. Due to the large deformation of impact, geometric nonlinearity is considered, and impact time is set to 200 μs.

Taking Case 1 and 2 as an example, the sequence of multi-layer composite is set considering their physical properties for improving the protection effectiveness. The first layer CFRP is a lightweight and high specific strength material. After penetrating the first layer, the bullet crushes the second layer (ceramics). The ceramic has high hardness and strength. It absorbs the energy of the bullet by deformation and damage. Finally, with high stiffness and support performance, UHMWPE and CFRP layers stop splatted shrapnel.

The stress contours of each layer of the multi-layer composite plates in Case 1, Case 2, Case 3 and Case 4 when the velocity of the bullet reaches minimum are shown in Figs. 4–7, respectively. The stress contours of the bullet when the velocity of the bullet reaches minimum in Case 1, Case 2, Case 3 and Case 4 are shown in Fig. 8.

For Case 1 and 2, the first CFRP layer and the Al₂O₃ Ceramic were penetrated after being impacted by the bullet, while the UHMWPE layer was not. The second CFRP layer is stretched out and broken with a hole because of the large deformation conducted from the UHMWPE layer. It demonstrated that the multi-layer composite plate of Case 1 and 2 is not penetrated and satisfies the bullet-proof requirements. For Case 1, the maximum stress of the first CFRP layer, Al₂O₃ ceramic, UHMWPE and the second CFRP layer are approximately 1198, 4467, 390 and 629 MPa, respectively. The maximum stress of the bullet is approximately 1484 MPa. For Case 2, the maximum stress of the first CFRP layer, Al₂O₃ ceramic, UHMWPE and the second CFRP layer are approximately 1047, 4869, 391 and 1017 MPa, respectively. The maximum stress of the bullet is approximately 1483 MPa. The Al₂O₃ ceramic layer plays a crucial role in absorbing the bullet's energy in the protective plates. The UHMWPE layer absorbs the attenuated bullet fragments and stops the bullet because of its high toughness.
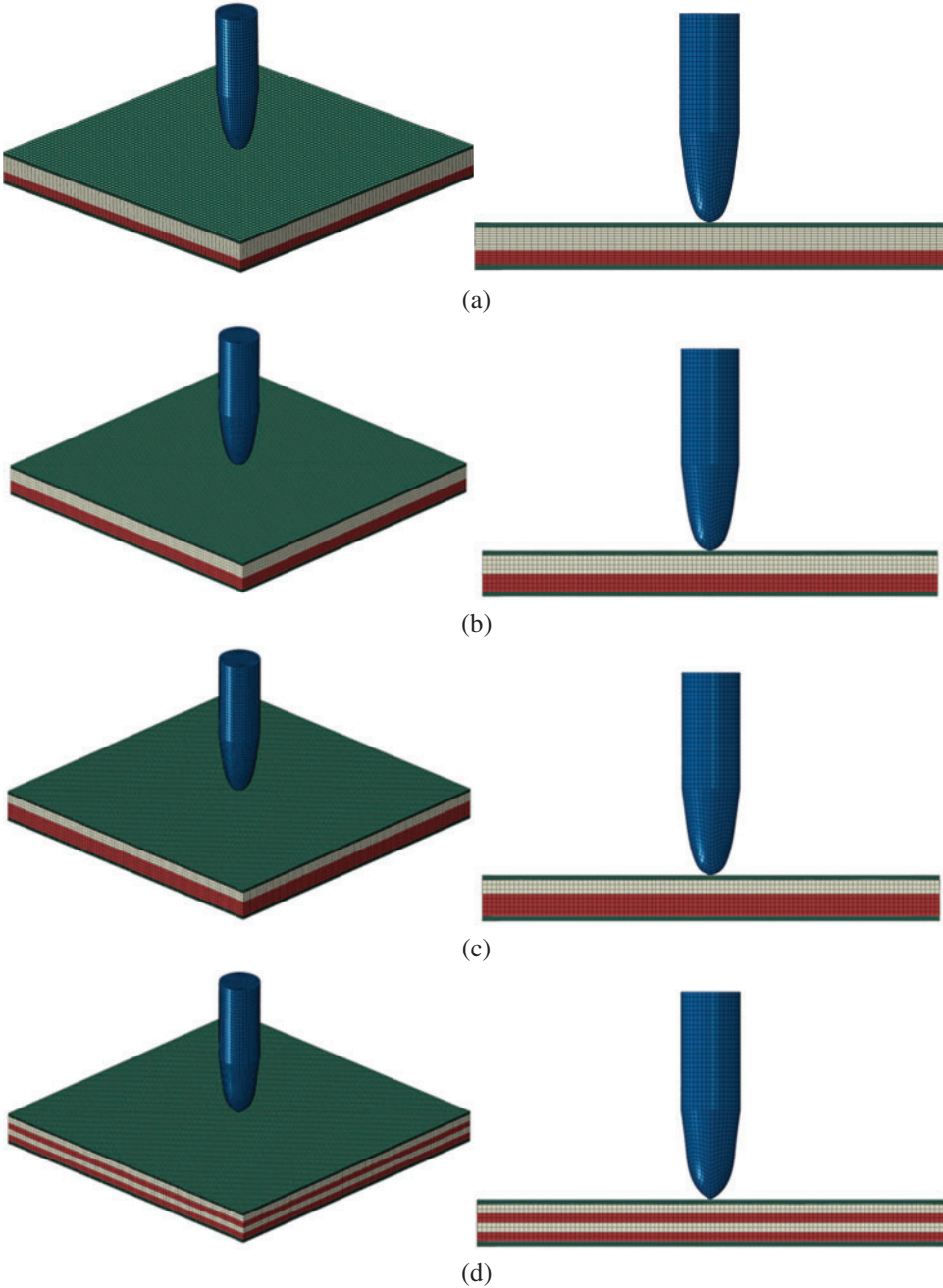
(a)

(b)

(c)

(d)

Figure 3: The finite element models in Case 1~4: (a) Case 1, (b) Case 2, (c) Case 3, (d) Case 4
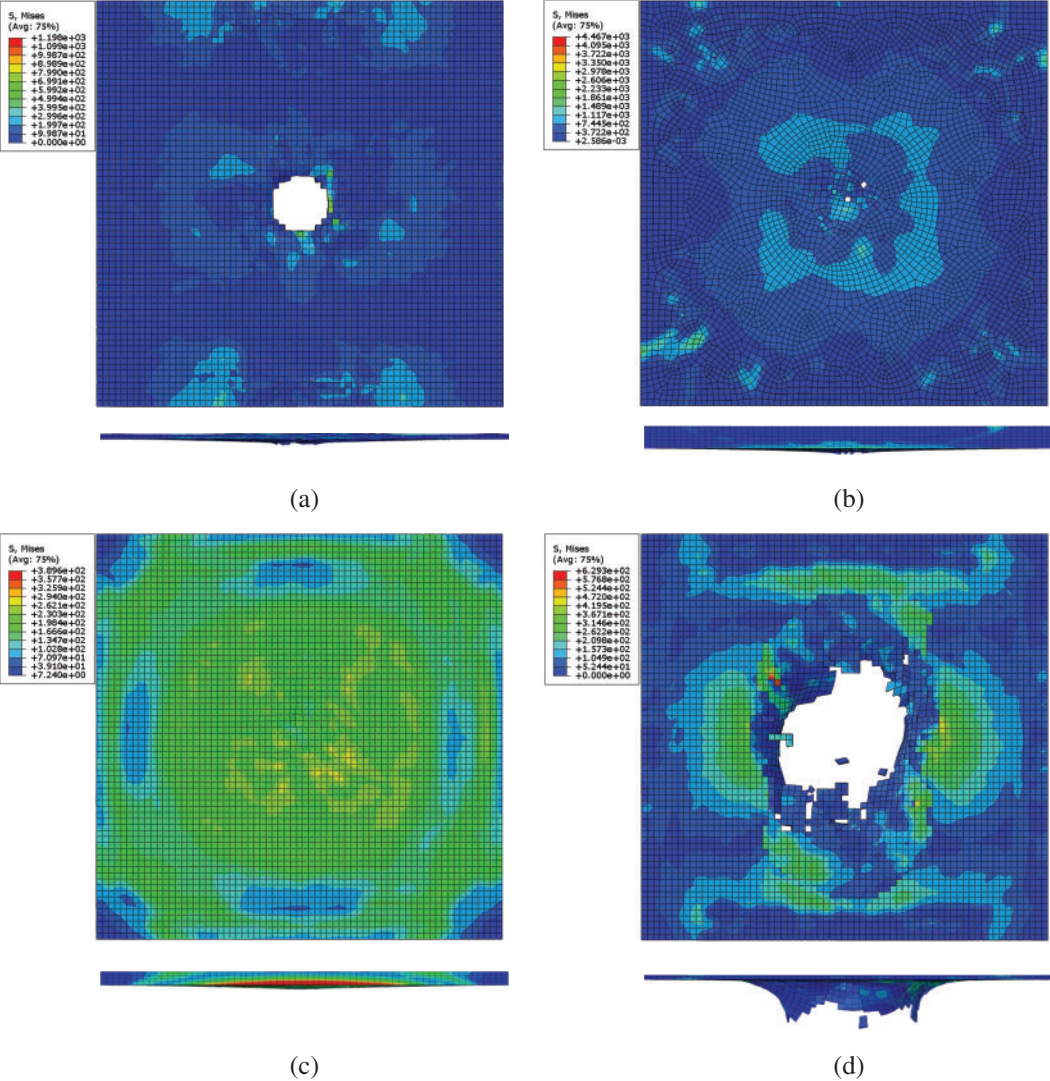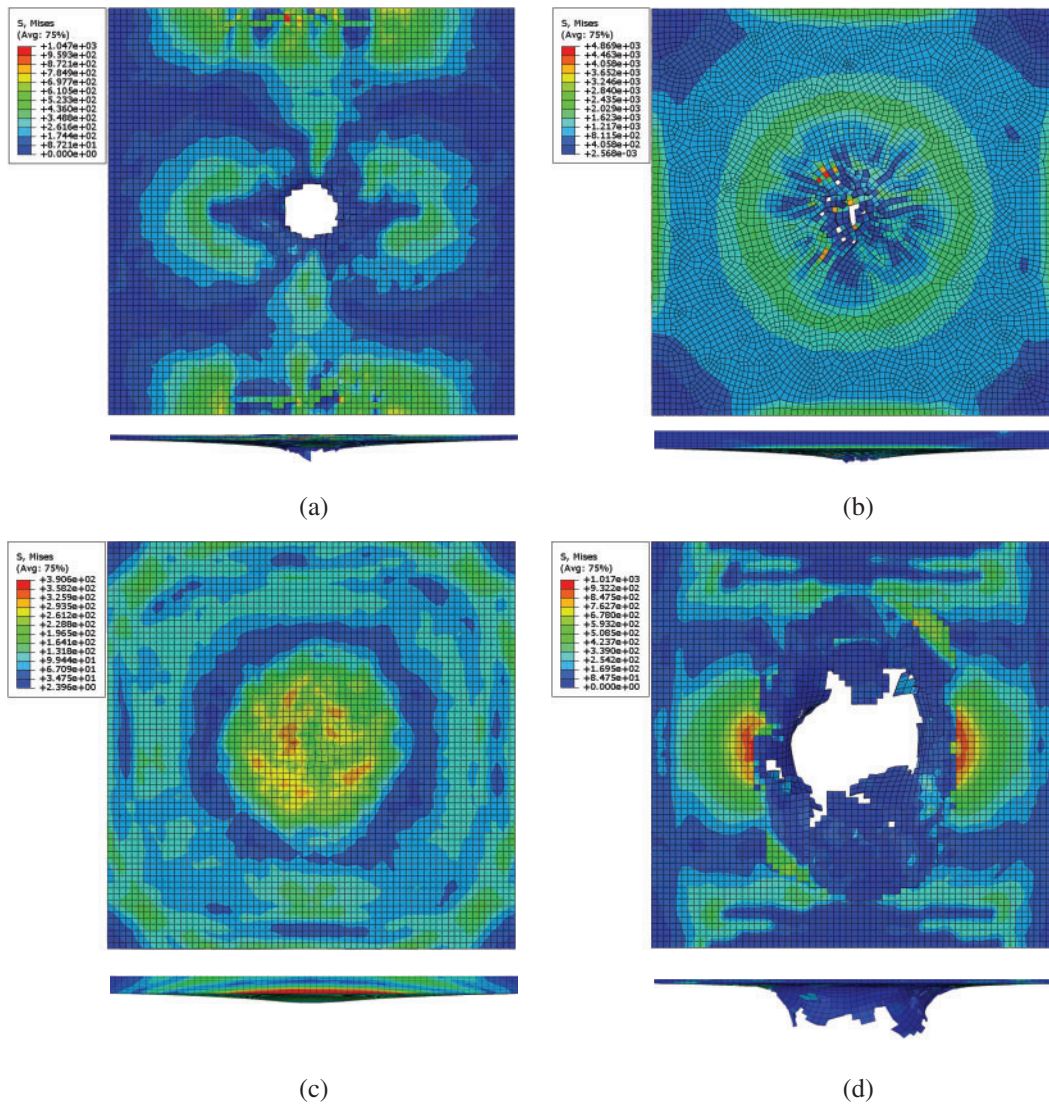
Figure 4: Stress contours of each layer when the velocity of the bullet reaches a minimum in Case 1: (a) First CFRP layer (1 mm), (b) Al_2O_3 Ceramic layer (5 mm), (c) UHMWPE layer (3 mm), (d) Second CFRP layer (1 mm) (Unit: MPa)

For Case 3, all the layers are broken with a hole after the bullet's impact. The UHMWPE layer is damaged partly and not penetrated throughout. It demonstrates that the bullet is embedded in the UHMWPE layer. The maximum stress of the first CFRP layer, Al_2O_3 ceramic, UHMWPE and the second CFRP layer are approximately 1424, 2766, 397 and 1212 MPa, respectively. The maximum stress of the bullet is approximately 1484 MPa. The bullet-proof performance of Case 2 is better than Case 3 shown in Table 5.

Figure 5: Stress contours of each layer when the velocity of the bullet reaches a minimum in Case 2: (a) First CFRP layer (1 mm), (b) Al_2O_3 Ceramic layer (4 mm), (c) UHMWPE layer (4 mm), (d) Second CFRP layer (1 mm) (Unit: MPa)

For Case 4, all the layers were penetrated throughout after being impacted by the bullet. The maximum stress of the first CFRP layer, the first Al_2O_3 ceramic layer, the first UHMWPE layer, the second Al_2O_3 ceramic layer, the second UHMWPE layer and the second CFRP layer are approximately 625, 2377, 390, 2314, 394 and 803 MPa, respectively. The maximum stress of the bullet is approximately 1435 MPa. The only difference between Case 2 and Case 4 is the sequences of the Al_2O_3 ceramic layer and the UHMWPE layer. It demonstrated that the first Al_2O_3 ceramic layer plays a crucial role in the bullet-proof process. Reducing the thickness of the first Al_2O_3 ceramic layer and placing it behind the UHMWPE layer will reduce the overall bullet-proof performance of the multi-layer composite. The maximum stress of the second UHMWPE layer is 1% higher than that of the first UHMWPE layer. The maximum stress of the second CFRP layer is 28% higher than that of the first CFRP layer.

It demonstrated that the maximum stress values in the first layers, which are in the later stages of bullet penetration, are reduced compared with those in the second layers in the earlier stages of bullet penetration.
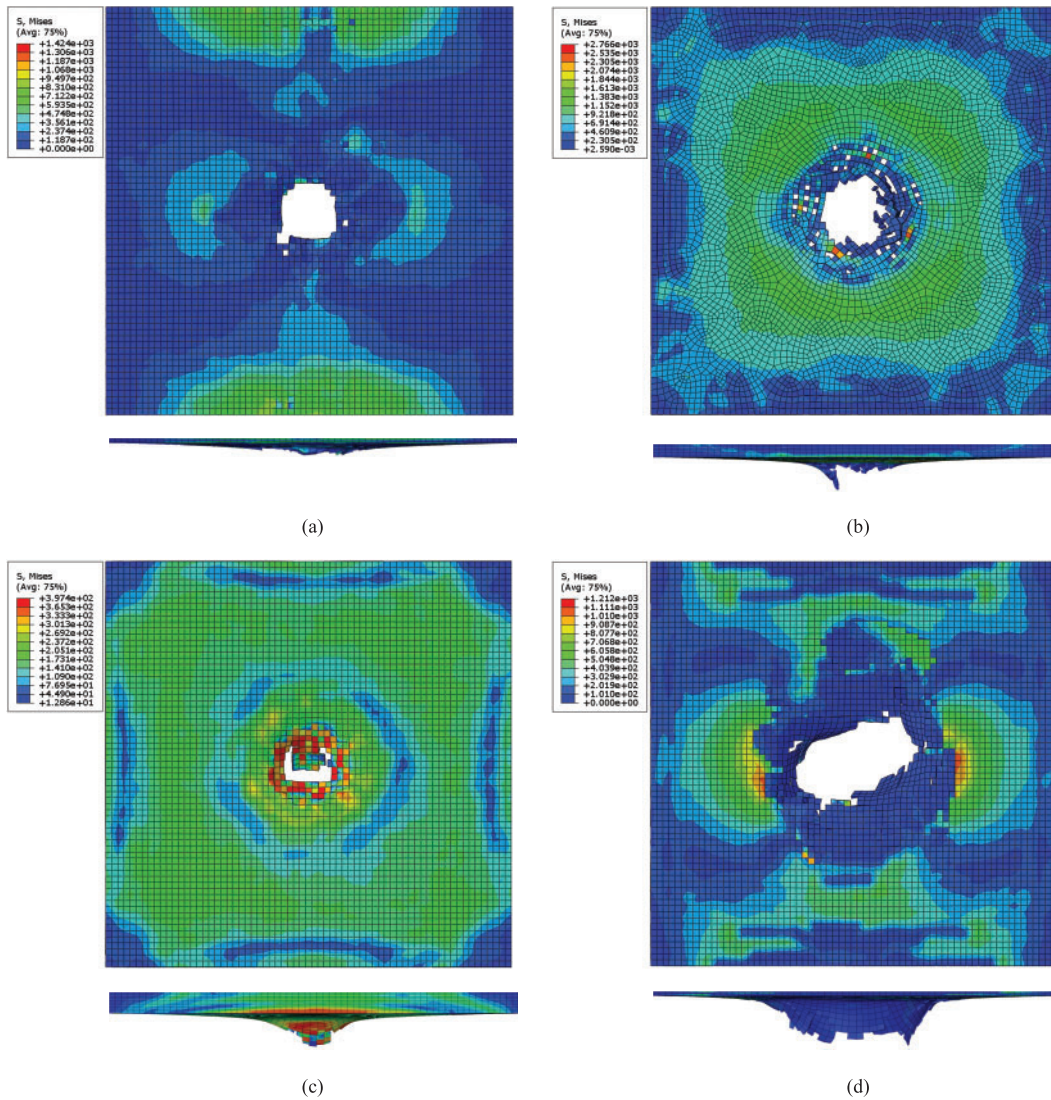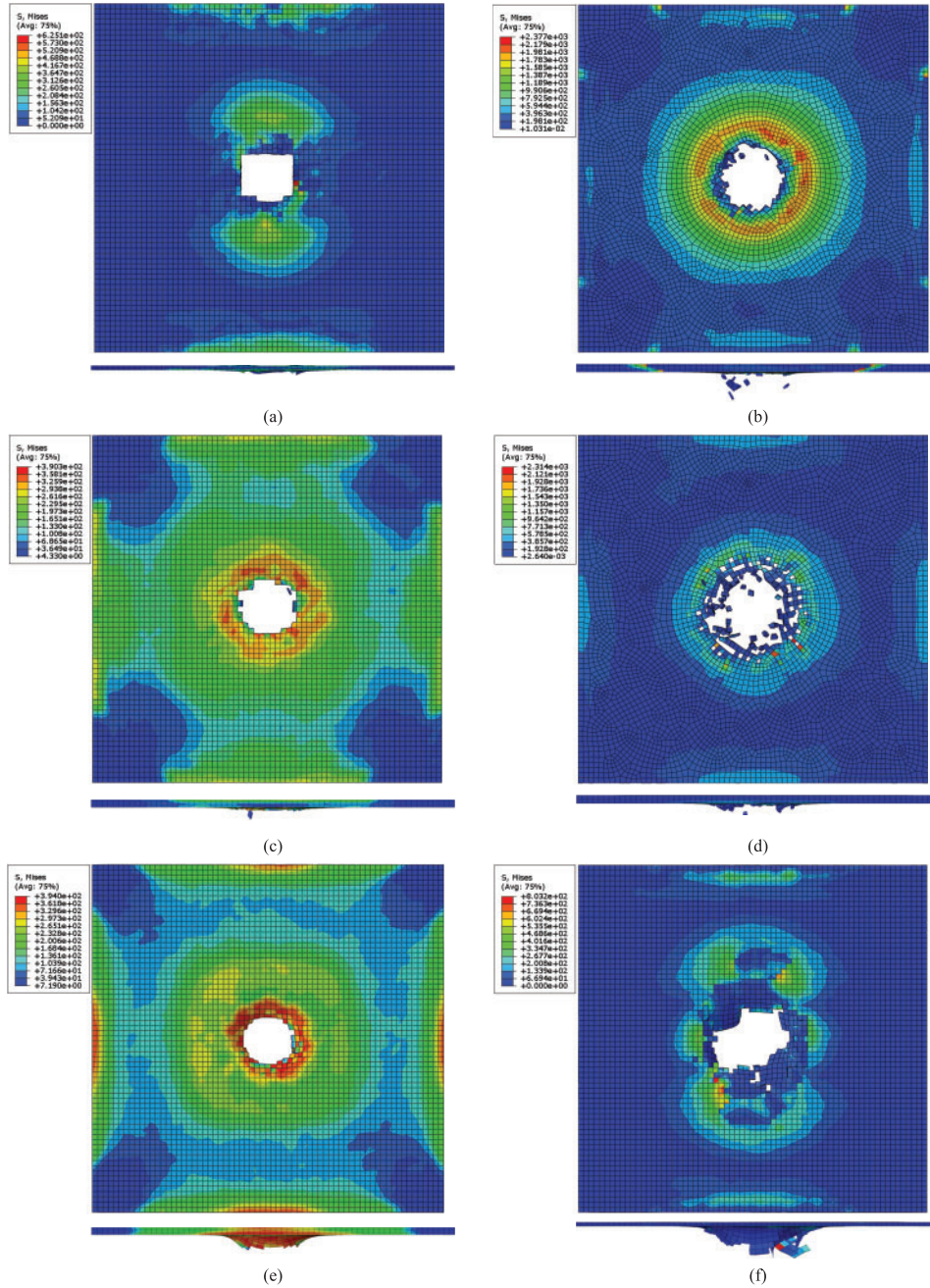

Figure 6: Stress contours of each layer when the velocity of the bullet reaches a minimum in Case 3: (a) First CFRP layer (1 mm), (b) Al_2O_3 ceramics layer (3 mm), (c) UHMWPE layer (5 mm), (d) Second CFRP layer (1 mm) (Unit: MPa)

Figure 7: Stress contours of each layer when the velocity of the bullet reaches a minimum in Case 4: (a) First CFRP layer (1 mm), (b) First Al_2O_3 ceramic layer (2 mm), (c) First UHMWPE layer (2 mm), (d) Second Al_2O_3 ceramic layer (2 mm), (e) Second UHMWPE layer (2 mm), (f) Second CFRP layer (1 mm) (Unit: MPa)
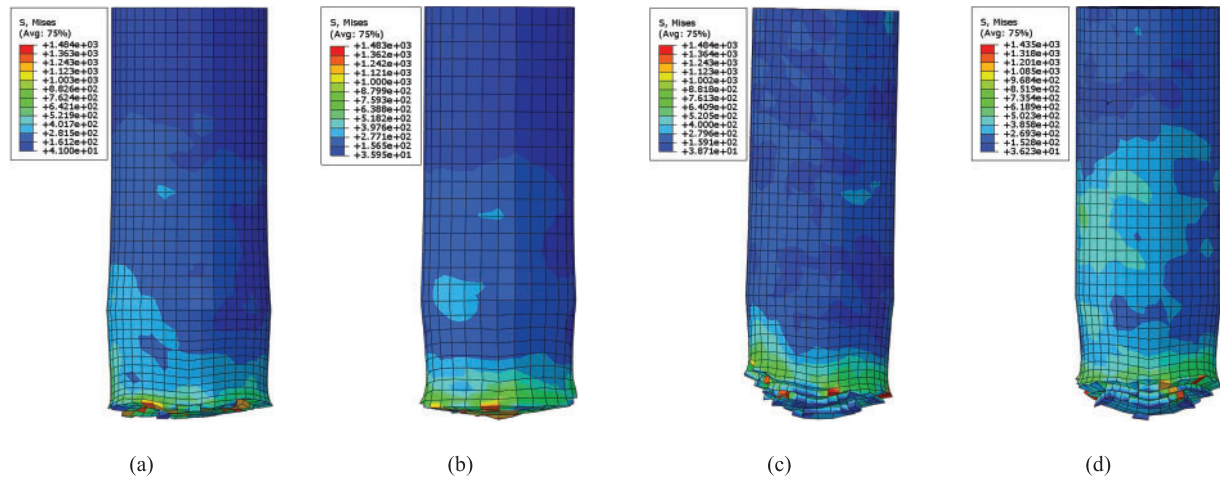
Figure 8: Stress contours of the velocity of the bullet reach a minimum in Case 1~4: (a) Case 1, (b) Case 2, (c) Case 3, (d) Case 4 (Unit: MPa)

Table 5: The maximum stress of each layer and the bullets in Case 1~4 when the velocity of the bullet reaches a minimum (Unit: MPa)

Case 1		Case 2		Case 3		Case 4	
CFRP	1198	CFRP	1047	CFRP	1424	CFRP	625
Ceramics	4467	Ceramics	4869	Ceramics	2766	Ceramics	2377
UHMWPE	390	UHMWPE	391	UHMWPE	397	UHMWPE	390
CFRP	629	CFRP	1017	CFRP	1212	Ceramics	2314
						UHMWPE	394
						CFRP	803
bullet	1484	bullet	1483	bullet	1484	bullet	1435

The inorganic-organic multi-layer bionic configuration is inspired by the structural mechanics of a white clam shell, which comprises lamellar thick calcium carbonate ($CaCO_3$) and thin organic matter (protein and polysaccharide) [9,12,13]. The above simulation results, showing the superior performance of Case 1 and Case 2 (thick Al_2O_3 ceramic and thin UHMWPE), confirm the effectiveness of the bionic mechanism of the white clam shell. Figs. 9–12 show the displacement contour of the multi-layer composite plates of Case 1, Case 2, Case 3 and Case 4, respectively.

Figs. 9a, 10a, 11a and 12a are the displacement contours at the start of impact in 0 μs. Figs. 9b, 10b, 11b and 12b show the displacement contour when the bullet velocity reaches a minimum in 82, 94, 102 and 62 μs, respectively. Figs. 9c, 10c, 11c and 12c are the displacement contours at the end of impact in 200 μs.
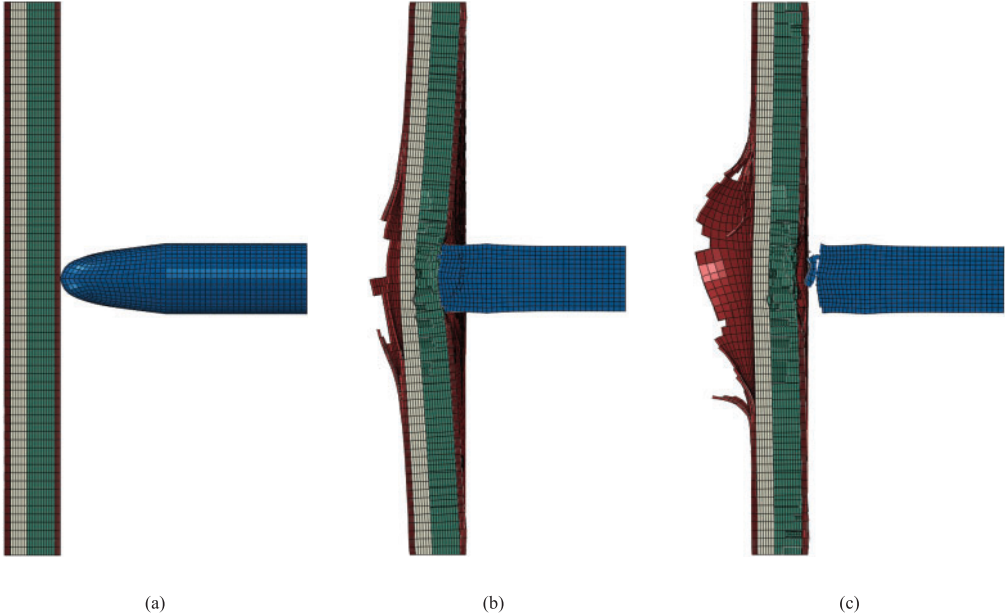
(a)   (b)   (c)

Figure 9: The displacement contour of the multi-layer composite plate in Case 1 at different moments: (a) The beginning of impact simulation (0 μs), (b) The velocity of the bullet reaches a minimum (82 μs), (c) The end of impact simulation (200 μs)
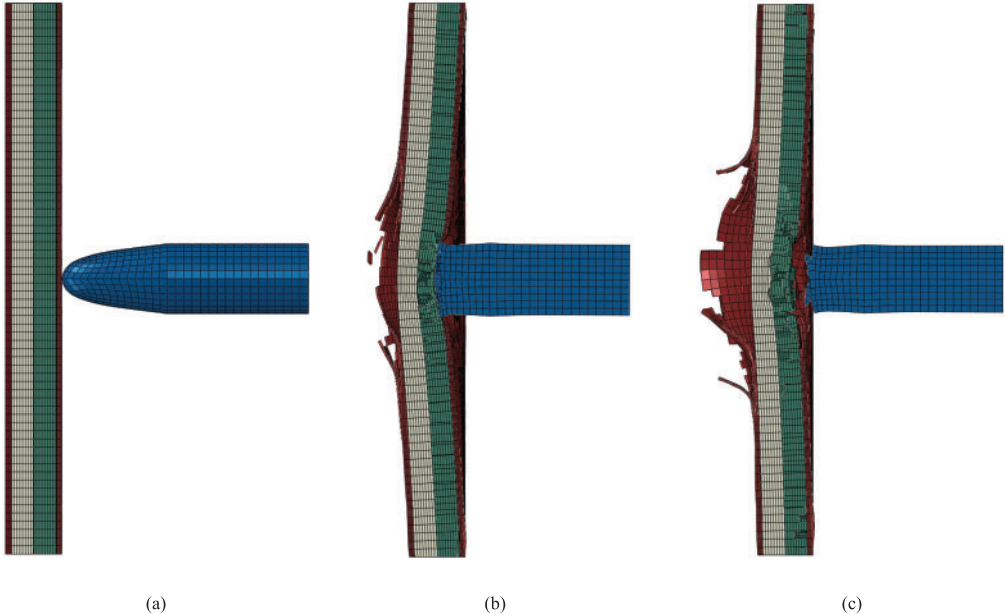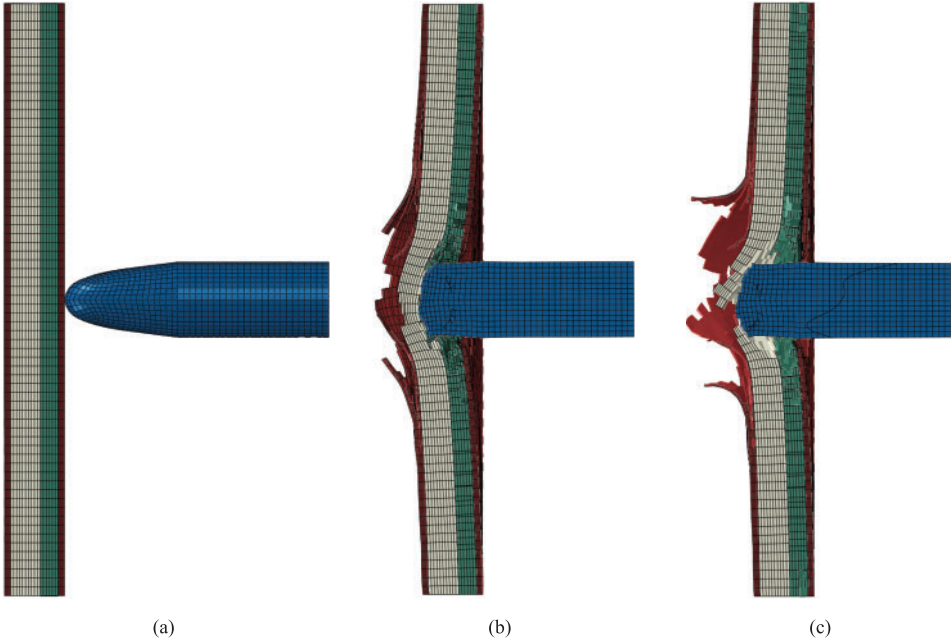

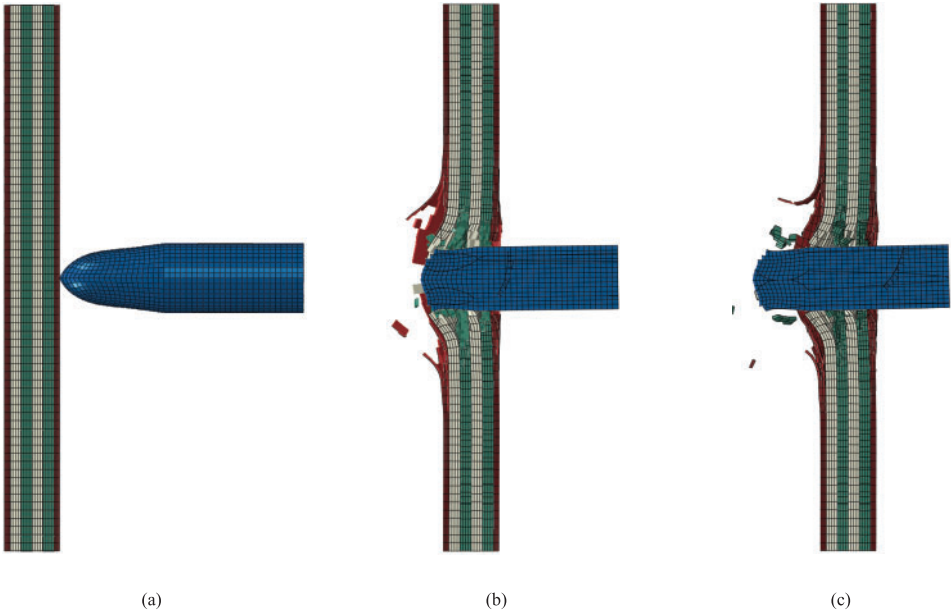(a)   (b)   (c)

Figure 10: The displacement contour of the multi-layer composite plate in Case 2 at different moments: (a) The beginning of impact simulation (0 μs), (b) The velocity of the bullet reaches a minimum (94 μs), (c) The end of impact simulation (200 μs)

Figure 11: The displacement contour of the multi-layer composite plate in Case 3 at different moments: (a) The beginning of impact simulation (0 μs), (b) The velocity of the bullet reaches a minimum (102 μs), (c) The end of impact simulation (200 μs)

Figure 12: The displacement contour of the multi-layer composite plate in Case 4 at different moments: (a) The beginning of impact simulation (0 μs), (b) The velocity of the bullet reaches a minimum (62 μs), (c) The end of impact simulation (200 μs)

Significant damage occurred at the central point after impact. Thus, the displacement history of the damaged flying splinters at the centre point cannot reflect the energy change of the composite plates. Therefore, a displacement recording point P rather than the central point at the back side of the last layer of the UHMWPE plate is selected for displacement comparison in Case 1~4. The displacement recording point is located at the point P in Fig. 1a in the last layer of the UHMWPE plate's surface on which the bullet exited. Fig. 13 illustrates the displacement history of the point P. The maximum displacements of the point P of Case 1~4 are recorded as 3.59, 3.80, 5.46 and 0.05 mm at 82, 94, 102 and 62 µs, respectively. The displacement in Case 4 is significantly less than in Case 1~3. Case 3 shows the most significant maximum displacement because the kinetic energy of the bullet is fully absorbed by the composite plate, while Case 4 shows the most minor maximum displacement because the composite plate is thoroughly penetrated by the bullet and the remaining kinetic energy of the bullet is the largest. Also, the time of the maximum displacement is increased from Case 4 to Case 1 to Case 2 to Case 3, aligning with the values of the maximum displacement.
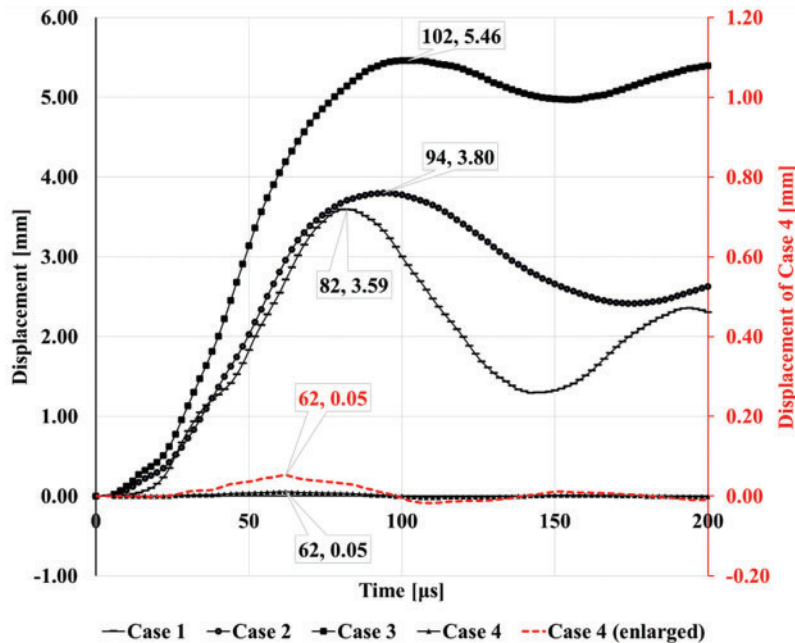

Figure 13: Displacement history of point P on the right side of the multi-layer composite plate in Case 1, Case 2, Case 3 and Case 4

Figs. 14–17 show the bullets' velocity and kinetic energy history during impact. After the bullet's velocity in Case 1 and Case 2 decreased to 0 m/s, the bullet rebounded with a constant velocity of approximately 60 and 40 m/s, respectively. In Case 3, the plate experiences substantial deformation and the appearance of cracks at the impact point, although it neither rebounds nor gets penetrated. The value of kinetic energy after the rebounding is close to 47 kJ. The bullet's velocity decreased to 0 m/s and is embedded on the plate with 0 kJ kinetic energy. For Case 4, the plate was penetrated throughout by the bullet at an exit velocity of 195 m/s with 511 kJ kinetic energy, the kinetic energy of the bullet is not fully transferred to the composite plate. The impact time, velocity of the bullet, kinetic energy and other parameters in Case 1~4 are listed in Table 6. It is concluded that the bullet-proof performance of Case 2 is optimal except for the overweight Case 1.
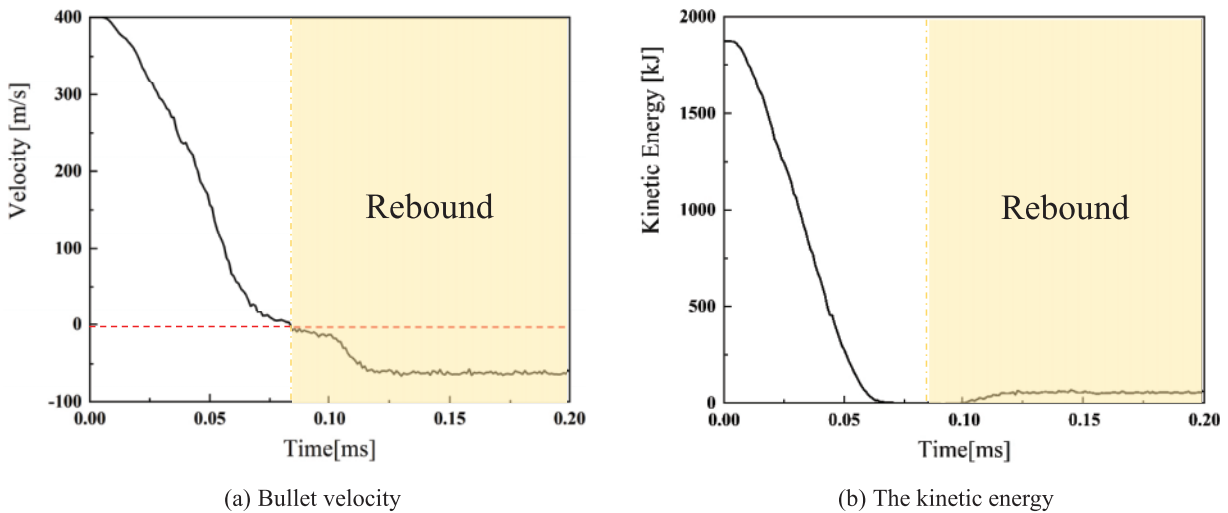
(a) Bullet velocity   (b) The kinetic energy

Figure 14: The history of the bullet's velocity and kinetic energy during the impact of Case 1

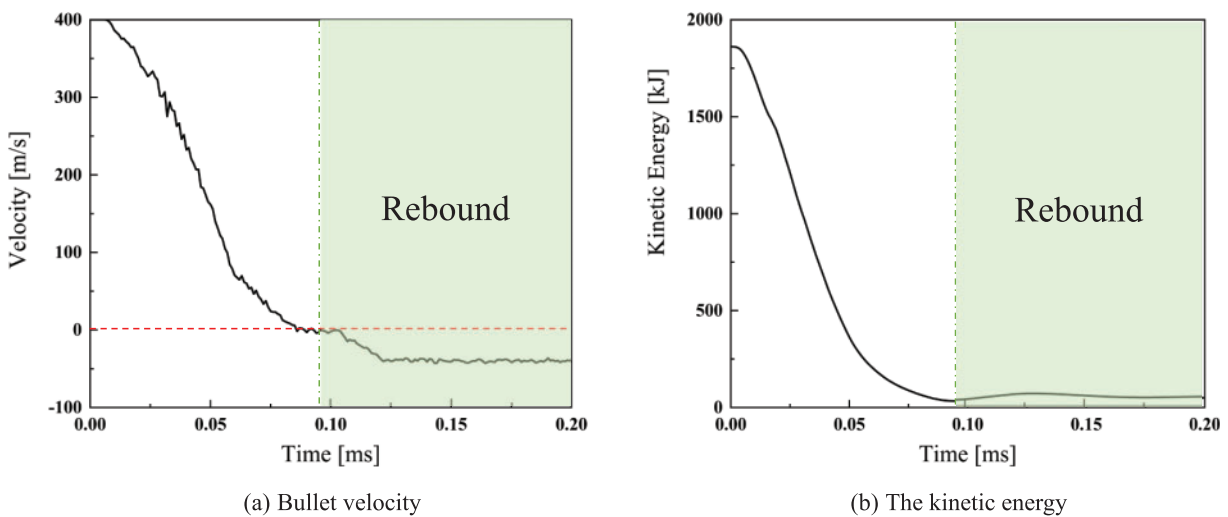(a) Bullet velocity   (b) The kinetic energy

Figure 15: The history of the bullet's velocity and kinetic energy during the impact of Case 2

3 Experiment

3.1 Fabrication

Taking Case 3 in Fig. 2 as an example, the Al_2O_3 ceramic layer is placed upon the CFRP and UHMWPE layers with sticky membrane films between each adjacent layer. After putting another CFRP layer, the CFRP out of the boundary is tailored. The stack sequence of the placed multi-layer composite sample is shown in Fig. 18. After pumping the vacuum, those placed layers of plates were put into an autoclave (see Fig. 19a) and heated to 195°C for 150 min, which makes sticky membrane films sticky (see Fig. 19b). After being printed in black colour, the formed multi-layer composite is shown in Fig. 20.
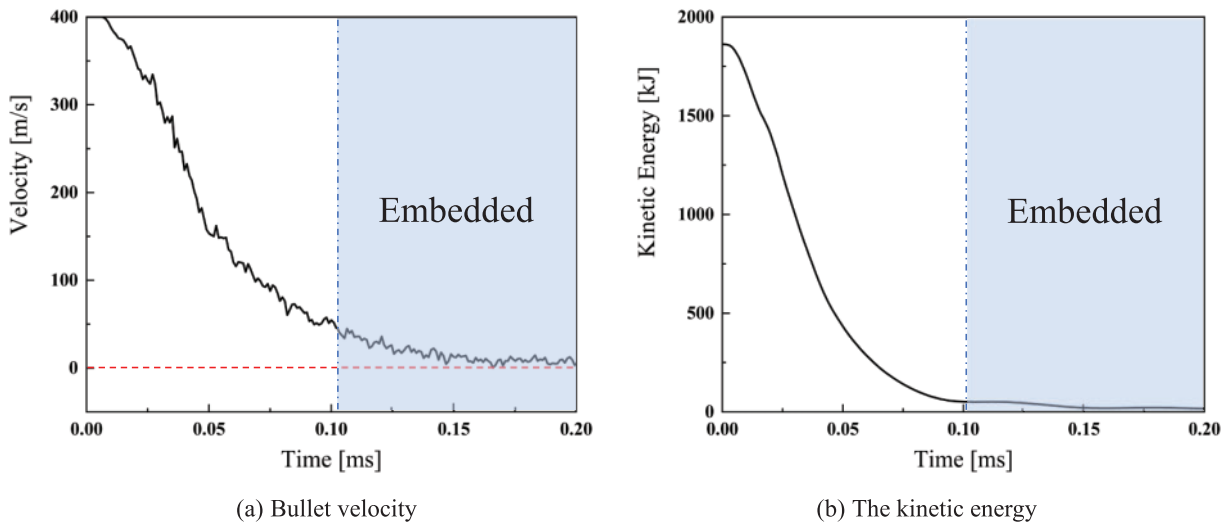
(a) Bullet velocity

(b) The kinetic energy

Figure 16: The history of the bullet's velocity and kinetic energy during the impact of Case 3
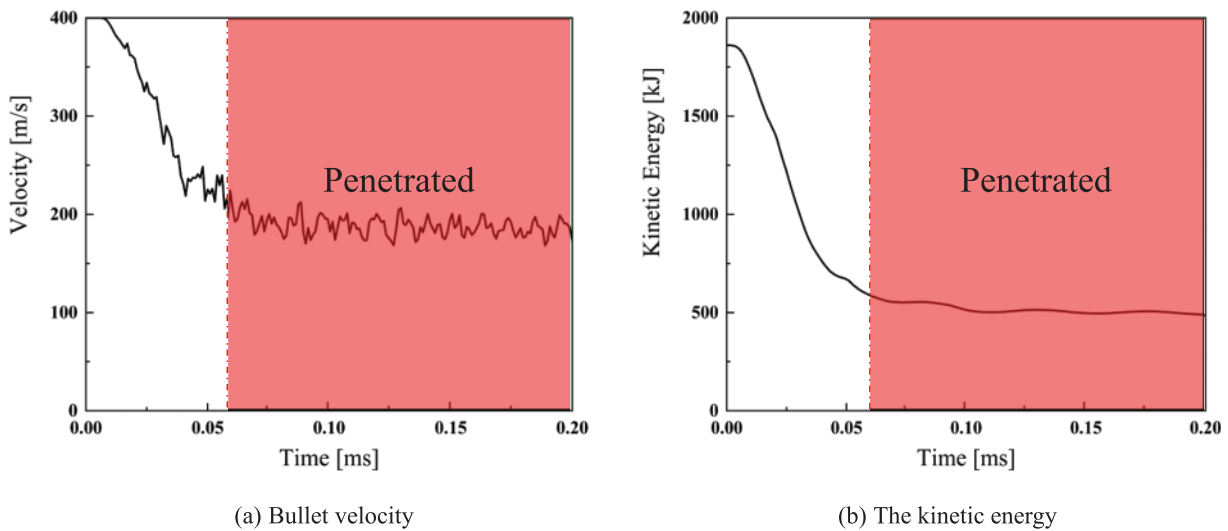

(a) Bullet velocity

(b) The kinetic energy

Figure 17: The history of the bullet's velocity and kinetic energy during the impact of Case 4

Table 6: The parameters of the bullets and plates during the impact in Case 1~4

	Case 1	Case 2	Case 3	Case 4
The start of the simulation	0 μs	0 μs	0 μs	0 μs
The time when bullet's velocity is minimum	82 μs	94 μs	102 μs	62 μs
The end of the simulation	200 μs	200 μs	200 μs	200 μs
The maximum displacement of point *P*	3.59 mm	3.80 mm	5.46 mm	0.05 mm

(Continued)

Table 6 (continued)

	Case 1	Case 2	Case 3	Case 4
The bullet velocity after the impact	−60 m/s	−40 m/s	0 m/s	195 m/s
The bullet's kinetic energy after the impact	106 kJ	47 kJ	0 kJ	511 kJ

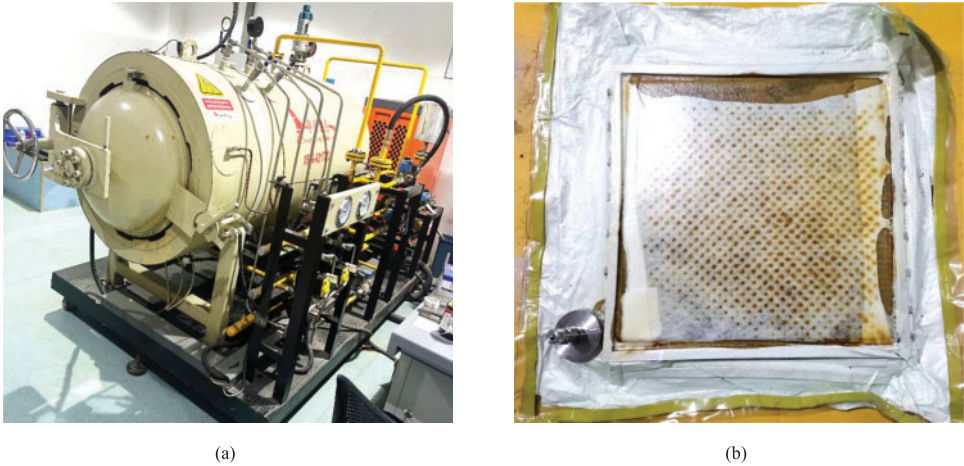
Figure 18: The stack sequence of multi-layer composite

Figure 19: The fabrication of multi-layer composite: (a) the autoclave, (b) the formed multi-layer composite

3.2 Ballistic Test

In this section, in order to verify the bullet-proof properties and the simulation results and provide guidance for composite design, the multi-layer composite samples in Case 2∼4 (see Table 1) were impacted in the China North Industries Group Corporation Limited Northwest Institute of Mechanical & Electronical Engineering. The 12.7 mm API is used as a bullet with a velocity of 400 m/s. The deviation of speed should be guaranteed within 30 m/s. The samples were fired from a gun at a distance of 4.3 m with an incident angle of 0°.
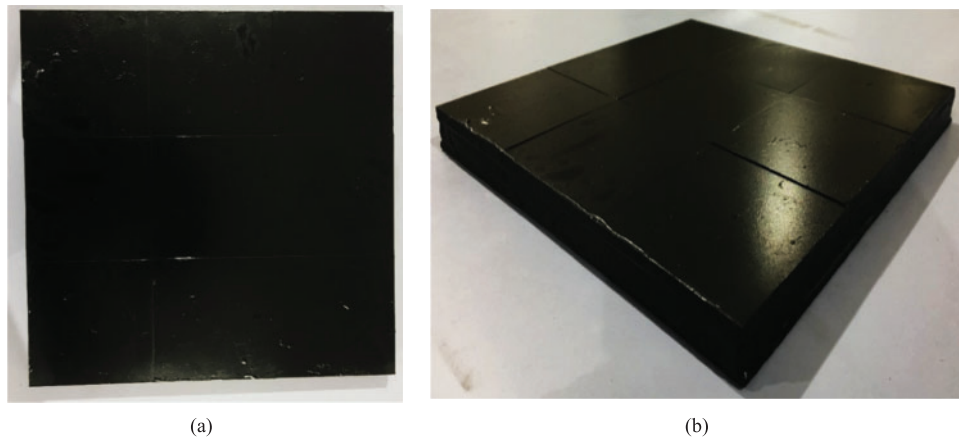
(a)   (b)

Figure 20: Test sample of the multi-layer composite after printed in black color: (a) top view of the sample, (b) oblique view of the base

The platform for high-speed impact tests is built according to MIL-STD-662E standards [48]. The ballistic test platform consists of a fixed base, a chronoscope, a velocity measurement target, a baffle, and a ballistic gun, as shown in Fig. 21. Two velocity measurement targets can record the time the bullet passes. Thus, the bullet's velocity can be calculated by the distance of targets and passed time. Since the bullet impact has high speed, the strain gauges attached to the surface of the composite plate were damaged and fell off under the influence of shock waves. Thus, the strain gauges cannot measure the strain change at the time of the bullet impact. The impact test carried out by the China North Industries Group Corporation Limited Northwest Institute of Mechanical & Electronical Engineering is a valid way to verify the effectiveness of simulation according to literature about the bullet-proof test [48,56–59].
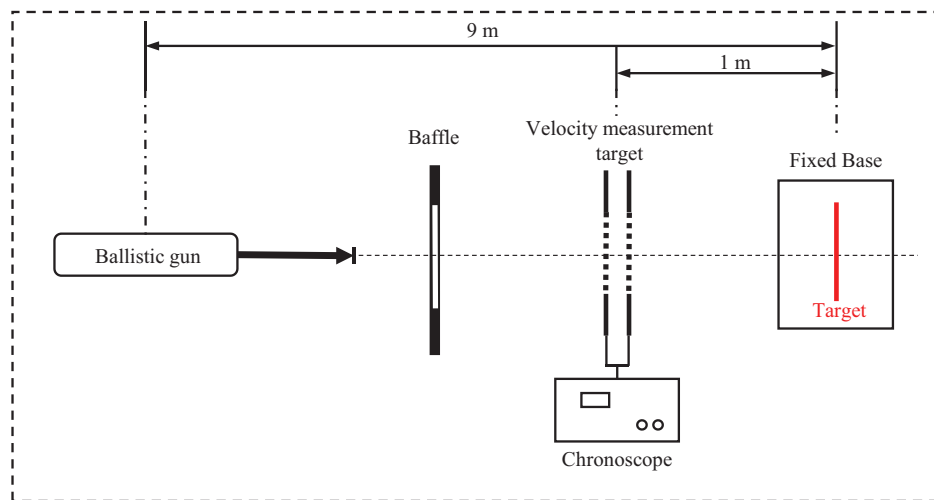

Figure 21: Schematic diagram of ballistic experiment

In the test, the three multi-layer composite samples in Case 2~4 (see Table 1) were fired $3 \times 4 = 12$ times, of which $3 \times 3 = 9$ times was effective fire, and the rest $1 \times 3 = 3$ times were speed calibration, bullet jamming, etc. Fig. 22 shows the appearance of the test samples in Case 2~4 after being impacted

by the bullets. Samples of Case 2 and Case 3 show the mosaic situation since it is not penetrated, while that of Case 4 is penetrated. The bullet-proof tests show the same result as the simulation results.
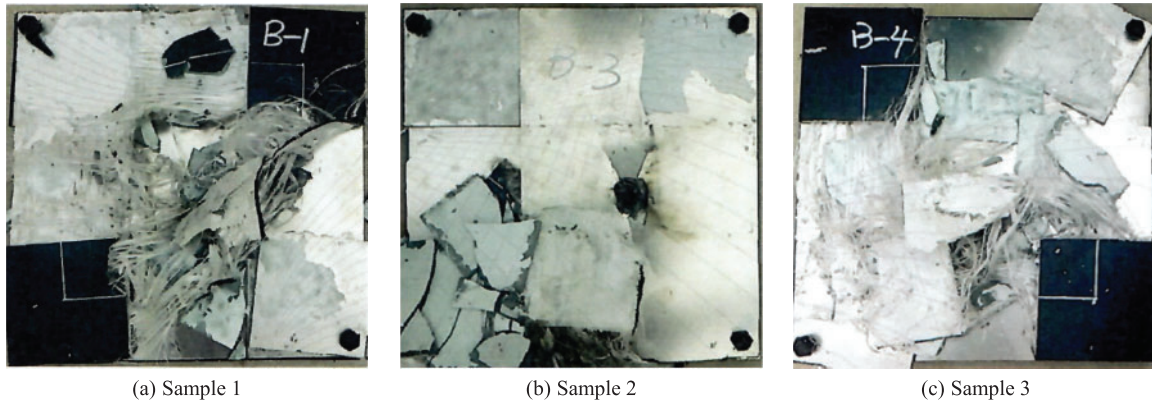

(a) Sample 1   (b) Sample 2   (c) Sample 3

Figure 22: Failure patterns of composite armor

4 Conclusions

In this study, a series of multi-layer protective armour with different sequences and thicknesses of materials impacted by a 12.7 mm armour-piercing incendiary (API) were designed, modelled, simulated, fabricated and tested. Based on the results obtained in the present work, the following main summary remarks and conclusions can be drawn:

1. A geometry model has been constructed for the multi-layer composite plates. To mimic the architecture of the white clam shell which comprises of lamellar thick calcium carbonate ($CaCO_3$) and thin organic matter (protein and polysaccharide), four cases with different layer sequences and thicknesses are modelled.

2. The impact of the abovementioned multi-layer composite plates by a 12.7 mm armor-piercing projectile, incident normally, is simulated using an explicit and nonlinear dynamic Abaqus finite-element analysis, to assess the potential of the four composite plates for use in ballistic-armor applications. The above simulation results, showing superior performance of Case 1 and Case 2 (thick Al_2O_3 ceramic and thin UHMWPE), confirm the effectiveness of the bionic mechanism of the white clam shell. The numerical results obtained from the 3D finite element models demonstrated the influences of the layer sequences and thicknesses and guided the optimum choice of the stack of the multi-layer composite.

3. The multi-layer composite was fabricated by pumping the vacuum into an autoclave and heating it to 195°C for 150 min.

4. The effectiveness of the simulation was verified by conducting the ballistic-proof test. For impact by a given real projectile at a fixed incident velocity in the China North Industries Group Corporation Limited Northwest Institute of Mechanical & Electronical Engineering, the stack of Case 1 (1 mm CFRP/4 mm Al_2O_3 ceramic/4 mm UHMWPE/1 mm CFRP) has the highest ballistic penetration resistance than other stacks. The simulation results with different layer sequences and thicknesses reasonably correlate with the experimental results.

The conclusions are helpful for the design of protective multi-layer structures. Future work needs to be done to study the concurrent design of the multi-layer structure and the motion of origami armor.

Author Contributions: The authors confirm contribution to the paper as follows: study conception and design: Dongsheng Jia; data collection: Liangdi Wang; analysis and interpretation of results: Dongsheng Jia, Yingjie Xu, Jihong Zhu; draft manuscript preparation: Dongsheng Jia, Weihong Zhang. All authors reviewed the results and approved the final version of the manuscript.

Availability of Data and Materials: The data that support the findings of this study are available from the first and corresponding authors upon reasonable request.

Conflicts of Interest: The authors declare that they have no conflicts of interest to report regarding the present study.

References

1. Brischetto, S., Torre, R., Cesare, D. (2023). Three dimensional coupling between elastic and thermal fields in the static analysis of multilayered composite shells. *Computer Modeling in Engineering & Sciences, 136(3),* 2551–2594. https://doi.org/10.32604/cmes.2023.026312

2. Kang, G., Ouyang, Q., Chen, P. (2023). Three-dimensional numerical manifold method for low-speed impact simulation of PBXs. *The International Conference on Computational Experimental Engineering and Sciences, 26(1),* 1. https://doi.org/10.32604/icces.2023.010508

3. Li, Z., Ji, J., Vu Quoc, L., Izzuddin, B. A., Zhuo, X. (2021). A 3-node no-rotational triangular finite element for non-Smooth, folded and multi-shell laminated composite structures. *Computer Modeling in Engineering & Sciences, 129(2),* 485–518. https://doi.org/10.32604/cmes.2021.016050

4. Ma, K., Liu, Z., Zhang, X., Xiao, B., Ma, Z. (2021). Fabrication of high strength carbon nanotube/7055Al composite by powder metallurgy combined with subsequent hot extrusion. *Science China Technological Sciences, 64(5),* 1081–1091.

5. Huo, Y., Tian, Y., Pu, S., Shi, T., Xia, Q. (2021). Bilateral filter for the optimization of composite structures. *Computer Modeling in Engineering & Sciences, 127(3),* 1087–1099. https://doi.org/10.32604/cmes.2021.015694

6. Xu, S., Li, W., Li, L., Li, T., Ma, C. (2022). Crashworthiness design and multi-objective optimization for bio-inspired hierarchical thin-walled structures. *Computer Modeling in Engineering & Sciences, 131(2),* 929–947. https://doi.org/10.32604/cmes.2022.018964

7. Chen, X., Wang, D., Dou, W., Wang, Y., Yang, Y. et al. (2020). Design and manufacture of bionic porous titanium alloy spinal implant based on selective laser melting (SLM). *Computer Modeling in Engineering & Sciences, 124(3),* 1099–1117. https://doi.org/10.32604/cmes.2020.09619

8. Yang, W., Li, J., Yang, J., Wei, L. (2015). Numerical simulation of an experienced farmer lifting tubers of cassava for designing a bionic harvester. *Computer Modeling in Engineering & Sciences, 104(6),* 471–491. https://doi.org/10.3970/cmes.2015.104.471

9.   Liang, Y., Zhao, Q., Li, X., Zhang, Z., Ren, L. (2016). Study of the microstructure and mechanical properties of white clam shell. *Micron, 87,* 10–17.

10. Chen, P. Y., McKittrick, J., Meyers, M. A. (2012). Biological materials: Functional adaptations and bioinspired designs. *Progress in Materials Science, 57(8),* 1492–1704.

11. Wu, K., Ni, Y. (2023). Multiscale structural design and fracture control of high-performance biomimetic materials. *The International Conference on Computational Experimental Engineering and Sciences, 26(3),* 1–2.

12. Meyers, M. A., Chen, P. Y., Lin, A. Y. M., Seki, Y. (2008). Biological materials: Structure and mechanical properties. *Progress in Materials Science, 53(1),* 1–206.

13. Yang, W., Chen, I. H., Gludovatz, B., Zimmermann, E. A., Ritchie, R. O. et al. (2013). Natural flexible dermal armor. *Advanced Materials, 25(1),* 31–48.

14. Sun, J., Bhushan, B. (2012). Hierarchical structure and mechanical properties of nacre: A review. *RSC Advances, 2(20),* 7617–7632.

15. Ritchie, R. O. (2011). The conflicts between strength and toughness. *Nature Materials, 10(11),* 817–822.

16. Cartwright, J. H. E., Checa, A. G., Escribano, B., Sainz-Díaz, C. I. (2009). Spiral and target patterns in bivalve nacre manifest a natural excitable medium from layer growth of a biological liquid crystal. *Proceedings of the National Academy of Sciences of the United States of America, 106(26),* 10499–10504.

17. Meyers, M. A., Chen, P. Y., Lopez, M. I., Seki, Y., Lin, A. Y. M. (2011). Biological materials: A materials science approach. *Journal of the Mechanical Behavior of Biomedical Materials, 4(5),* 626–657.

18. Wang, Z., Sun, Y., Wu, H., Zhang, C. (2018). Low velocity impact resistance of bio-inspired building ceramic composites with nacre-like structure. *Construction and Building Materials, 169(2018),* 851–858.

19. Grujicic, M., Snipes, J. S., Ramaswami, S. (2016). Ballistic impact behavior of nacre-like laminated composites consisting of B_4C tablets and polyurea matrix. *Journal of Materials Engineering and Performance, 25(3),* 977–994.

20. Flores Johnson, E. A., Shen, L., Guiamatsia, I., Nguyen, G. D. (2014). Numerical investigation of the impact behaviour of bioinspired nacre-like aluminium composite plates. *Composites Science and Technology, 96(2014),* 13–22.

21. Miao, T., Shen, L., Xu, Q., Flores Johnson, E. A., Zhang, J. et al. (2019). Ballistic performance of bioinspired nacre-like aluminium composite plates. *Composites Part B: Engineering, 177(2019),* 107382.

22. Yang, H., Ren, Y. (2023). Crashworthiness design of CFRP/AL hybrid circular tube under lateral crushing. *Thin-Walled Structures, 186,* 110669.

23. Yang, H., Ren, Y. (2023). Crushing behavior of CFRP/AL hybrid tubes under oblique lateral loading. *Polymer Composites, 44(10),* 6403–6418.

24. Jiang, H., Wang, Y., Ren, Y. (2022). Controllable energy-absorption behaviors of the perforated CFRP tube with an adhesively bonded CFRP patch. *Thin-Walled Structures, 181,* 110015.

25. Jiang, H., Liu, X., Jiang, S., Ren, Y. (2023). Hybrid effects and interactive failure mechanisms of hybrid fiber composites under flexural loading: Carbon/Kevlar, carbon/glass, carbon/glass/Kevlar. *Aerospace Science and Technology, 133,* 108105.

26. Vecchio, K. S. (2005). Synthetic multifunctional metallic-intermetallic laminate composites. *JOM Journal of the Minerals Metals and Materials Society, 57(3),* 25–31.

27. Chandler, M. Q., Sherburn, J. A., Allison, P. G., Moser, R. D., Torres-Cancel, K. A. et al. (2017). Application of bio-inspired nanocomposites for enhancing impact resistance of cementitious materials. *International Journal of Impact Engineering, 110,* 171–180.

28. Lin, G. (2023). Low-velocity impact response of sandwich composite panels with shear stiffening gel filled honeycomb cores. *The International Conference on Computational Experimental Engineering and Sciences*, vol. 26, no. 3, pp. 1–2. https://doi.org/10.32604/icces.2023.09075

29. Hilmes, R. (1987). *Brassey's multilingual military dictionary*. London: Brassey's Defence Publishers.

30. Santos, V. C., Lopes, P. S., Gärtner, R., Jorge, A. B. (2007). Weight and reliability optimization of a helicopter composite armor using dynamic programming. *The International Conference on Computational Experimental Engineering and Sciences*, vol. 4, no. 2, pp. 53–58.

31. Ramadhan, A. A., Talib, A. R. A., Rafie, A. S. M., Zahari, R. (2012). The Influence of impact on composite armour system kevlar-29/polyester-Al_2O_3. *IOP Conference Series: Materials Science and Engineering, 36(1),* 012028. https://doi.org/10.1088/1757-899X/36/1/012028

32. Hur, H. K., Kim, M. S. (2010). Ballistic resistance of multi-layered sandwich composites. *51st AIAA/ASME/ASCE/AHS/ASC Structures, Structural Dynamics and Materials Conference*, Orlando, Florida, USA.

33. McDaniels, K., Downs, R. J., Meldner, H., Beach, C., Adams, C. (2009). High strength-to-weight ratio non-woven technical fabrics for aerospace applications. *AIAA Balloon Systems Conference*, Seattle, Washington, USA.

34. Chiou, C. P., Margetan, F. J., Barnard, D. J., Hsu, D. K., Jensen, T. et al. (2012). Nondestructive characterization of UHMWPE armor materials. *AIP Conference Proceedings*, pp. 1168–1175. Burlington, USA.

35. Soydan, A. M., Tunaboylu, B., Elsabagh, A. G., Sarı, A. K., Akdeniz, R. (2018). Simulation and experimental tests of ballistic impact on composite laminate armor. *Advances in Materials Science and Engineering, 2018,* 4696143.

36. Chen, Y. L., Huang, W. K., Yeh, J. N. (2021). Theoretical analysis of bulletproof capability of multilayer ceramic composites subjected to impact by an armor piercing projectile. *Advances in Materials Science and Engineering, 2021,* 9922229.

37. Feli, S., Asgari, M. R. (2011). Finite element simulation of ceramic/composite armor under ballistic impact. *Composites Part B: Engineering, 42(4),* 771–780.

38. Wang, K., Li, M., Yan, P., Dong, L. (2022). An experimental and numerical study on the ballistic performance of multi-layered moderately-thick metallic targets against 12.7-mm projectiles. *Computer Modeling in Engineering & Sciences, 131(1),* 165–197. https://doi.org/10.32604/cmes.2022.019188

39. Hassouna, A., Mezlini, S., Ben Ameur, T. (2023). Numerical study of ballistic impact of hard bulletproof vests: Effect of the multilayered armors design. *Polymer Composites, 44(12),* 8496–8509.

40. Goda, I., Girardot, J. (2021). Numerical modeling and analysis of the ballistic impact response of ceramic/composite targets and the influence of cohesive material parameters. *International Journal of Damage Mechanics, 7(30),* 1079–1122.

41. Yin, G. X., Li, W. B., Huang, X. N., Zhang, K. B., Hong, D. et al. (2023). Ballistic performance study of multilayer Al_2O_3 ceramic-metal composite armor under strong confinement. *Journal of Physics: Conference Series, 2478(7),* 072011.

42. Voiculescu, I., Geanta, V., Chereches, T., Vizureanu, P., Stefanoiu, R. et al. (2022). Impact behavior of the ballistic targets package composed of dyneema polymer and high entropy alloy structures. *Archives of Metallurgy and Materials, 67(2),* 569–576.

43. Hu, P., Cheng, Y., Zhang, P., Liu, J., Yang, H. et al. (2021). A metal/UHMWPE/SiC multi-layered composite armor against ballistic impact of flat-nosed projectile. *Ceramics International, 47(16),* 22497–22513.

44. Signetti, S., Ryu, S., Pugno, N. M. (2022). Impact mechanics of multilayer composite armors: Analytical modeling, FEM numerical simulation, and ballistic experiments. *Composite Structures, 297,* 115916.

45. Alam, S., Shakar, S. (2021). Ballistic impact performance of triangular corrugated core sandwich composite armor. *International Journal of Composite Materials, 11(2),* 23–35.

46. Jia, D., Feng, P., Wang, L., Chen, L., Wang, J. et al. (2023). An origami shield with supporting frame structures optimized by a feature-driven topology optimization method. *Defence Technology, 31,* 447–456. https://doi.org/10.1016/j.dt.2023.02.022

47. Johnson, G. R., Holmquist, T. J. (1994). An improved computational constitutive model for brittle materials. *AIP Conference Proceedings*, pp. 981–984. Colorado, USA.

48. MIL-STD-662F (1997). *Military standard: V50 ballistic test for armor*. USA: US Military Specs/ Standards/Handbooks.

49. Johnson, G. R., Cook, W. H. (1985). Fracture characteristics of three metals subjected to various strains, strain rates, temperatures and pressures. *Engineering Fracture Mechanics, 21(1),* 31–48.

50. Holmquist, T. J., J. G., Cook, W. H. (1995). A computational constitutive model for concrete subjected to larger strains, high strain rates and high pressure. *The 14th International Symposium on Ballistics*, pp. 591–600. Quebec, Canada.

51. Wang, Y., Liu, Z. G., Wei, Y. C., Li, Z. J., Yi, Y. P. et al. (2020). Novel processing technology and mesoscopic geometric modeling of a new three-dimensional (3D) braided composite and the study on its longitudinal mechanical properties. *Composite Structures, 251,* 112525.

52. Wang, Y., Liu, Z. G., Yi, Y. P., Wei, Y. C., Li, Z. J. et al. (2021). Damage and failure analyses of 3D4d braided composite shafts under torsional load and the effects of braid processing parameters on their torsional properties. *Polymer Composites, 42(4),* 1912–1944.

53. Gu, X., Su, X., Wang, J., Xu, Y., Zhu, J. et al. (2020). Improvement of impact resistance of plain-woven composite by embedding superelastic shape memory alloy wires. *Frontiers of Mechanical Engineering, 15(4),* 547–557.

54. Hashin, Z. (1980). Failure criteria for unidirectional fiber composites. *Journal of Applied Mechanics, 47(2),* 329–334.

55. Nie, Z. (2014). *Advanced mesomechanical modeling of triaxially braided composites for dynamic impact analysis with failure (Ph.D. Thesis)*. The University of Akron, USA.

56. Guo, Y. N. (2016). *Research on the ballistic impact behavior and configuration of ceramic faced composite armor (Ph.D. Thesis)*. Northwestern Polytechnical University, China.

57. Peng, G., Wang, M., Feng, J. C, Liu, Y. D., Wang, X. C. (2011). Research on the application of ballistic limit velocity V50 to the evaluation of bullet-proof performance of materials. *Police Technology, (2),* 12–15.

58. Miao, T., Shen, L., Xu, Q., Flores-Johnson, E. A., Zhang, J. et al. (2019). Ballistic performance of bioinspired nacre-like aluminium composite plates. *Composites Part B: Engineering, 177,* 107382.

59. Wang, Z., Sun, Y., Wu, H., Zhang, C. (2018). Low velocity impact resistance of bio-inspired building ceramic composites with nacre-like structure. *Construction and Building Materials, 169,* 851–858.